Study of ice nucleation on silver iodide surface with defects

Prerna, Rohit Goswami, Atanu K. Metya, S. V. Shevkunov & Jayant K. Singh

Taylor & Francis
Taylor & Francis Group

CUMMINGS SPECIAL ISSUE

Check for updates

Study of ice nucleation on silver iodide surface with defects

Prerna[a], Rohit Goswami [a], Atanu K. Metya[a], S. V. Shevkunov[b] and Jayant K. Singh[a]

[a]Department of Chemical Engineering, Indian Institute of Technology Kanpur, Kanpur, India; [b]Peter the Great St. Petersburg Polytechnic University, St. Petersburg, Russia

ABSTRACT

In this work, we have considered the crystallisation behaviour of supercooled water in the presence of surface defects of varying size (surface fraction, α from 1 to 0.5). Ice nucleation on Ag exposed β-AgI (0001 plane) surface is investigated by molecular dynamics simulation at a temperature of 240 K. For systems with $\alpha > 0.67$, the surface layers crystallise within 150 ns. In the system with defects, we observe two distinct stacking patterns in the layers near the surface and find that systems with AA stacking cause a monotonic decrease in the early nucleation dynamics with an increase in defect size. Where AB stacking ($\alpha = 0.833$) is observed, the effect of the defect is diminished and the dynamics are similar to the plain AgI surface. This is supported by the variation in the orientational dynamics, hydrogen bond network stability, and tetrahedrality with respect to the defects. We quantify results in terms of the network topology using double-diamond cages (DDCs) and hexagonal cages (HCs). The configurations of the initially formed layers of ice strongly affect the subsequent growth even at long timescales. We assert that the retarded ice growth due to defects can be explained by the relative increase in DDCs with respect to HCs.
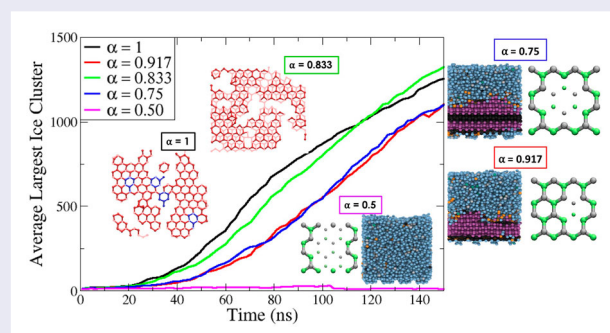
Statement of significance

Silver iodide is a common material used for the acceleration of the rare ice nucleation event. Existing studies have probed the effect of diverse factors including structural anomalies during precipitation, charge distribution and surface flexibility. The present study addresses the gap in the understanding of supercooled systems with defects on the surface. We quantify the effect of defects of increasing size in terms of the structural changes which are observed close to the surface in terms of template mismatches. The methodology described herein demonstrates a holistic approach to understanding near-surface structural changes in terms of variations in nucleating ability.

1. Introduction

Ice nucleation is a prevalent natural phenomenon, but is convoluted and poorly understood [1]. Over the years, several studies have been conducted to understand this process [2], however a complete understanding of the intricacies of the underlying mechanism remains elusive. From industrial processes like cryopreservation [3–5], lyophilisation [6], waste-water treatment [7,8] to the

natural events like hail and rainfall [9,10], the phase transition is an essential stride in many operations [11,12] such as cloud seeding for weather modification [13], parameterisation of climate modelling [14,15]. Nonetheless, the economic and environmental hazards of ice accretion on airplanes [16], infrastructure elements like railway tracks, power lines [17], etc. cannot be disregarded. Based on the applications and previous studies, nucleation approaches can be stratified [18] as (i) freezing strategies which focus on speeding up as well as controlling the nucleation rate, (ii) anti-freezing strategies necessitate inhibition of nucleation process [19–21] in order to prevent its detrimental effects. Nucleation of water occurs either through homogeneous or heterogeneous nucleation depending on the presence of impurities. In the upper troposphere of the Earth's atmosphere, droplets of pure liquid water under supercooled conditions have been found to undergo homogeneous nucleation at a temperature close to $-40°C$ [22]. While at a warmer temperature, the concentration of foreign matter acts as a catalyst and expedite the nucleation process by virtue of heterogeneous nucleation [23]. One of the principal effects of heterogeneous nucleation can be discerned in clouds which comprise of a diverse variety of foreign particles. Mineral dust, volcanic ashes, biological and carbonaceous aerosol shows varied composition [24] and temperature dependency towards ice nucleation [25], which further influences precipitation, radiation budget, and climate [26]. Hence, investigations into the effect on ice nucleation due to these particles are essential to capture their impact on climate.

So far, extensive experimental studies [27–29] have been conducted for identification of active nucleation sites in addition to understanding the ice nucleation mechanism and quantifying ice nucleation ability. However, due to timescale and length scale restrictions, it is challenging to achieve a molecular-level understanding of the nucleation mechanism through experimental exercises [30]. Recently, ice nucleation of supercooled water over surfaces with diverse properties and unique nucleation mechanism, such as carbon-based surfaces [31–34], aerosol particles like silver iodide [14], as well as wide range of mineral dusts like quartz, feldspar and clays [25], biological particles [35,36], etc. have been investigated using atomistic and coarse-grain simulations. These studies show that a slight change in surface properties could accelerate or impede nucleation tendency. Heterogeneous ice nucleation has also been found to be susceptible to structural variation with respect to the surface [37,38]. Our groups have previously investigated various aspects of nucleation such as nucleation rate, work of adhesion, freezing temperature [39] on rough

and smooth surfaces and demonstrated the linearity of freezing temperature and work of adhesion with corresponding roughness based on wetting state [40]. The study of lubricant impregnated textured surface inferred that ice adhesion strength augments with increasing texture density [41]. The impact of the nanotextured surface on ice nucleation has also been explored in terms of wetting states (Cassie-Baxter and Wenzel state) and the surface fraction [42].

Among all the ice-nucleating agents, silver iodide (AgI) is widely used as cloud seeding agents because of its efficacious ice-nucleating ability [43]. Owing to this efficiency, diverse experimental and theoretical studies [29,44] have been devoted to the ice nucleation on AgI surface. Zielke *et al.* [38] observed that silver exposed AgI surface accelerated ice nucleation while iodide exposed surface hindered the process. Water condensation studies over β-AgI surface with defects in the form of rectangular towers [45] and pyramids [46,47] showed greater thermodynamic stability of condensate over the surface. The increased stability at the early stage of nucleation was reported to be a function of the shape and size of the nanostructure [45]. Similar condensation study over AgI surface with disordered structure observed an increase in absorption ability [48] and rupture of the hydrogen bond between molecules due to defects [46,48]. However, the influence of defective AgI surface on the liquid to solid transition mechanism of water has not been probed using molecular dynamics (MD). Recent studies have reported enhanced ice nucleation efficiency for systems with surface defects in the form of steps, cavities, and crevices [27]. The nucleation rate has been reported to increase for surface geometries which favour the formation of topological defects in ice lattice structures [49].

In this study, our objective is to capture how defects on silver iodide surface induce orientational variation during the early stages of nucleation. We have considered the AgI surface incorporated with the defects of varying sizes. MD simulation has been conducted for the all-atom system of water and surface. In simulations, typical classification techniques based on spherical harmonics [50] have been well established for use for bulk systems [51,52]. Previous work [53] has attempted to characterise stability and structure in terms of closed path structures or 'rings', however recent work [54,55] has proven the utility and relevance of graph traversal techniques for characterisation. For systems which show heterogeneous nucleation, surface effects dominate during the initial nucleation period. We investigate the structural changes in the layers close to the surface with respect to the defects and correlate these changes to the early nucleation.

2. Model and simulation details

In this work, we have considered the Ag exposed face of β-AgI (0001 plane) as the surface for ice nucleation. The surface is modelled as the rigid lattice of Lennard-Jones (LJ) sites with positive and negative charges represented as silver and iodide atoms, respectively. Water molecules are represented by TIP4P/Ice [56] (melting point = 270 K) as it can capture the overall phase diagram and density of various ice forms efficiently [56]. The interactions between surface atoms and water are modelled using the 12-6 LJ potential and the electrostatic potential as given below:

$$U = \sum_{ij} 4\epsilon_{ij}\left[\left(\frac{\sigma_{ij}}{r_{ij}}\right)^{12} - \left(\frac{\sigma_{ij}}{r_{ij}}\right)^{6}\right] + \sum_{ij}\frac{Cq_iq_j}{r_{ij}} \quad (1)$$

where r_{ij} is the distance between i and j atoms, q_i and q_j are the charge on each i and j atom, respectively, C

Table 1. LJ parameters utilised in the simulation.

Pair	ϵ (kcal/mol)	σ (Å)
Ag–O	0.547	3.17
I–O	0.622	3.34
Ag–H	0.220	1.95
I–H	0.250	3.12

is Coulomb's constant. σ and ϵ are the LJ parameters for interaction between surface and water (mentioned in Table 1). The LJ parameters for AgI have been referred from Hale and Kiefer [57] excluding the polarisation contributions. A cutoff distance of 8.5 Å is considered for LJ interactions. The effect of surface charge variation has not been considered in this work and has been kept constant at ($\pm$)0.6 reduced units.

The AgI slab (four layers of AgI) is further incorporated with the structural defects by removing Ag and I atoms in pair from the top layer of the surface to model the natural defect on the surface. The whole AgI surface is divided into 12 unit cells after that from each unit cell a particular number of Ag and I atom pairs (1, 2, 3, 4, 5, and 6) are removed uniformly. This forms a superlattice as shown in Figure 1. The top view of the whole surface is given in Figure S1 of supplementary information. For characterising defect, the surface fraction (α) is defined as the ratio of the number of atoms on the topmost layer to the number of atoms in any other layer within the surface [42].

Each system comprises of 5120 water molecules loaded on AgI surface. The dimension of the simulation box is $55.18 \times 47.78 \times 250$ Å^3. This box is considered to be periodic in all directions with a vacuum (≈ 200 Å)
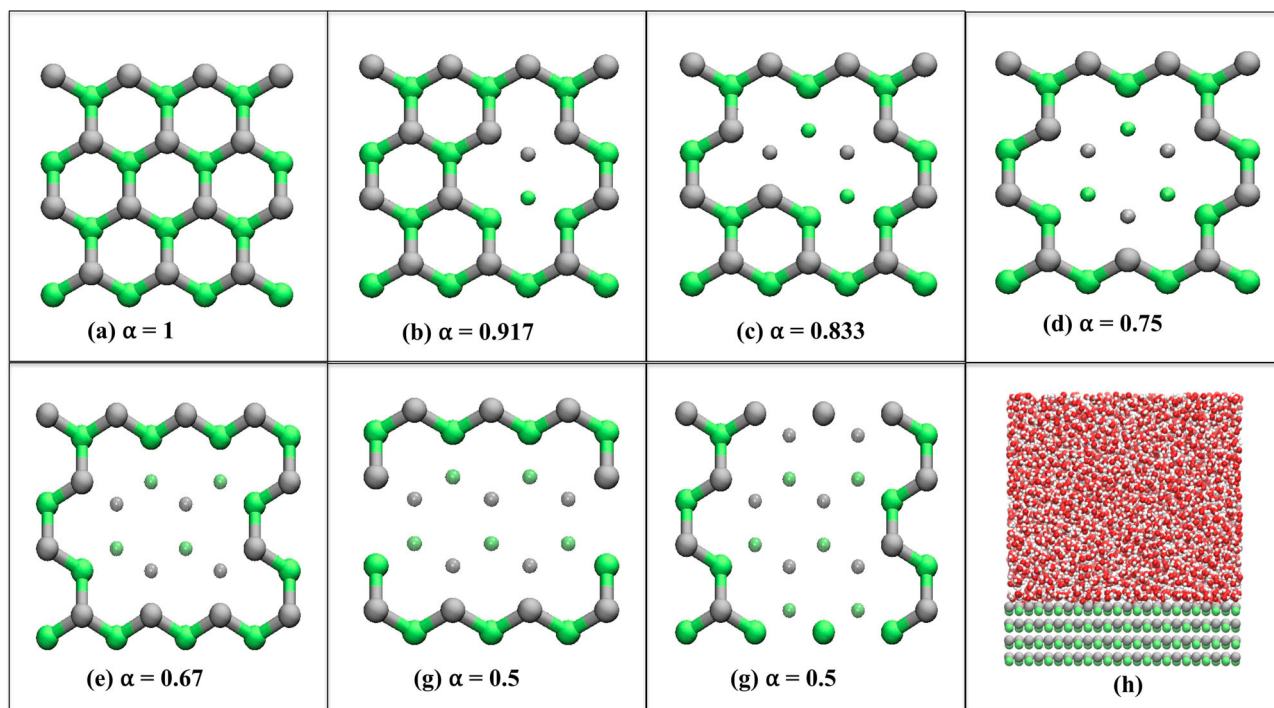

Figure 1. Top view of the unit cell of AgI surfaces incorporated with the defects of varying size. Silver and lime colours represent Ag and I, respectively, small atoms represent Ag and I atoms of the bottom layer. (a) Surface without defect ($\alpha = 1$), (b) surface with the smallest defect ($\alpha = 0.917$), (c) ($\alpha = 0.833$), (d) ($\alpha = 0.75$), (e) ($\alpha = 0.67$), (f) ($\alpha = 0.58$) and (g) surface with the largest defect ($\alpha = 0.5$). (h) Shows the simulation box of the system. The whole surface is shown in Figure S1 of the supplementary.

along z direction to avoid any nonphysical interactions between periodic images of the surface. All MD simulations are carried out under canonical ensemble (i.e. NVT ensemble with constant particle, volume, and temperature) using LAMMPS simulation package [58], and visual molecular dynamics (VMD) [59] was used for visualisation. The bond and the angle of the water molecule have been fixed by the SHAKE algorithm [60]. The surface is kept immobile for our simulations. For the integration of the equations of motion, the velocity Verlet algorithm is utilised. Long-range coulombic interactions are computed using Particle–Particle Particle–Mesh (PPPM) TIP4P kspace solver of LAMMPS with a precision of 10^{-4}. Nosé–Hoover thermostat [61,62] has been used to maintain constant temperature conditions with a relaxation time of 0.1 ps. Each system is first equilibrated at 300 K for 5 ns; after that multiple configurations are generated at the interval of 1 ns. These configurations are used as the starting point for independent simulations. The simulation initiates with quenching for 2 ns wherein the temperature is reduced from 300 K to 240 K followed by isothermal simulations at 240 K for 300 ns.

3. Methods

3.1. Dipole orientation

Previous studies [63,64] have proclaimed the correlation of water dipole orientation distribution and nucleation propensity of the surface. So, orientational analysis was conducted to study the effect on supercooled water arrangement close to surface for various defective substrates. This includes orientational distribution [63] which is the probability distribution of angle between water dipole vector and perpendicular to the surface (θ) as a function of $\cos\theta$. Furthermore, the orientational correlation function (C_{vv}) [65] was also calculated and the expression used is given as follows:

$$C_{vv}(t - t_0) = \langle \delta\vec{v}(t) \cdot \delta\vec{v}(t_0) \cdot \psi_i(t_0) \rangle \qquad (2)$$

where v is the unit vector along water dipole, t_o is the reference time, $\langle . \rangle$ symbolises the normalised ensemble average and ψ_i is either 1 if water molecule is within the considered layer at t_0 or else 0.

3.2. Early-time polymorph distribution

Early-time polymorph (ETP) distribution analysis [66] (i.e. I_c, I_h and interfacial ice composition within the largest ice cluster) was computed to assimilate the variation just before ice nuclei size grows rapidly. Bond-orientational order parameter q_3 [50,51] was used for

identification of ice-like molecules along with classifying cubic, hexagonal and interfacial ice structures. Details of the criteria used for ice polymorph classification have been mentioned in our previous work [42].

3.3. Topological analysis

The three-dimensional structure of ice may be clarified in terms of the network connectivity. This stems from the identification of the smallest building blocks of I_h and I_c. These can be obtained by following the graph traversal reduction techniques reported recently [54]. This methodology involves the determination of double-diamond cages (DDCs) and hexagonal cages (HCs). These DDCs are the building blocks of cubic ice, while HCs form hexagonal ice. The algorithm described also identifies geometries which may act as growth surfaces for either kind of ice, i.e. they are 'mixed cages' (MCs).

4. Results and discussion

In order to observe the influence of the surface defect on ice nucleation, we carried out the isothermal simulation at 240 K. First, we have evaluated the density distribution of water molecules over the various ranges of time (i.e. 5–15 and 80–90 ns) for the different defected AgI surface. Figure 2 presents the average number of water molecules along the normal direction to the surface. Before the onset of freezing (see Figure 2(A)), two major distinct peaks of the water molecules close to the AgI surface are observed for smaller defective substrate, i.e. $\alpha \geq 0.67$ (here, the centre position of the top layer of the surface is at 13.5 Å, marked by an indigo line in Figure 2). The first and second peak of water are located at 15.4 Å (in the first hydration layer, i.e. between 13.5 and 17 Å) and 18.2 Å (in the second hydration layer, i.e. between 17 and 20.5 Å), respectively. For the defect system, the water molecules penetrated within the defect of the surface. As the size of the defect increases the number of water molecules in the defect increases (see Table 2). At $\alpha < 0.67$, the broadening of water density profile (see Figure 2) clearly shows the absence of the ordering of water molecule on the top of the AgI surface. As the nucleation proceeds (80–90 ns, see Figure 2(B)), there is no significant change in the peak height of the first layer of water, whereas substantial changes in the peak height of the second layer for $\alpha \geq 0.67$ are observed. However, for $\alpha < 0.67$, no visible ordering of water molecules near the surface is observed. Thus, these surfaces inhibit the nucleation of water. Additionally, in the second hydration layer (for $\alpha \geq 0.67$), the distance between two peaks is 0.9 Å which is considered as the height of the chair formation hexagons in ice [63]. It is evident from the density profile that the peak height
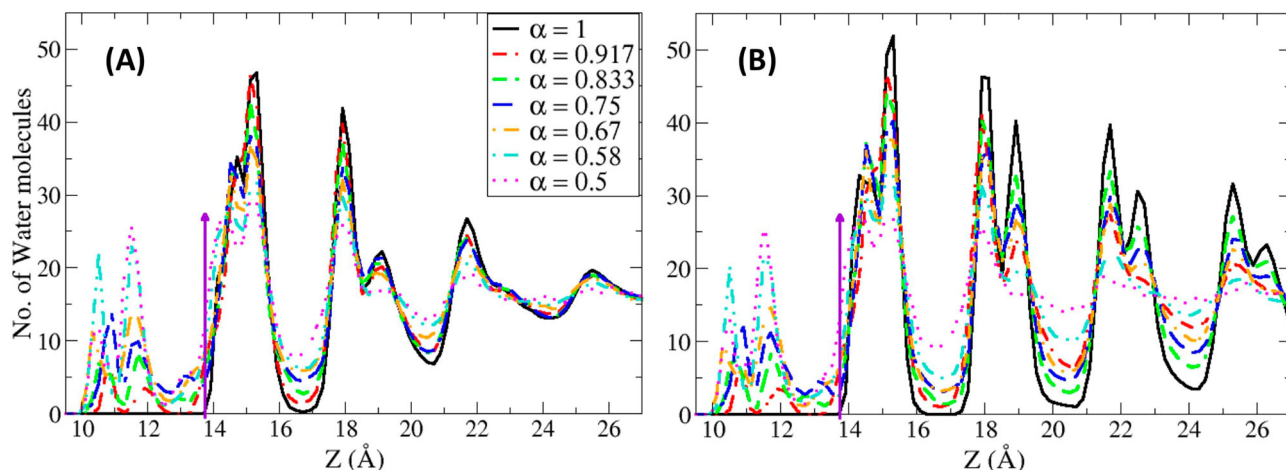
Figure 2. Density distribution along z-axis averaged over the following range of time (A) 5–15 ns and (B) 80–90 ns, the indigo arrow indicates the centre position of the top layer of AgI surface.

Table 2. Nomenclature and average number of water molecules within the defect of various systems.

Nomenclature	α	Avg. no. of water molecules in each defect
AgI-d0	1	0
AgI-d1	0.917	2
AgI-d2	0.833	4
AgI-d3	0.75	7
AgI-d4	0.67	8
AgI-d5	0.58	11
AgI-d6	0.5	12

decreases with the increasing surface defect size which indicates that the layering of water reduces with α (see the second hydration shell in Figure 2(B)).

Next, we have evaluated the in-plane radial distribution function (2D-RDF) [67] of water in the first and second hydration shells (i.e. 13.5–17 Å and 17–20.5 Å, respectively). The RDF plots (Figure 3(A,B)) clearly indicate that the position of the dominant first peak in the in-plane RDF appears at 2.75 Å which is inline with previous works. Before the onset of crystallisation, water molecules near the surface are strongly ordered in the first hydration shell (Figure 3A(I), except $\alpha <$ 0.67), whereas ordering of water molecules has not been observed in the second layer (see Figure 3B(I)). With progress in crystallisation (80–90 ns), there is no significant change in the RDF of first water layer (i.e. water molecules close to the surface) whereas the water molecules are more ordered in the second hydration shell which indicates ice formation (for $\alpha \geq$ 0.67). The height of the peaks in the RDF decreases slightly with increasing defect size in the AgI surface. This also supports that water molecules near the surface may affect the nucleation behaviour of supercooled water.

Figure 4 shows the average largest ice cluster size as a function of time averaged over 15 configurations. It is

clear that ice nucleates in the system with $\alpha \geq 0.67$. We did not observe nucleation in the system with $\alpha < 0.67$ up to 150 ns. The system with $\alpha = 0.67$ shows delay in nucleation and the largest ice cluster size remains below 250 molecules till 150 ns. Interestingly, we have found that the nucleation starts early in the system with $\alpha = 1$ and 0.833 (as compared to $\alpha = 0.917$ and 0.75). Similar trend is observed for the average overall ice-like molecules in the system with respect to the time. In order to understand above conjecture, the effect of the defects on initial ice polymorphs being formed close to the surface have been investigated using early-time polymorphs distribution. Figure 5 (left) presents I_c, I_h and interfacial ice distribution (distinguished using bond-orientational order parameter q_3 [50,51]) within the largest clusters having the size of 200 molecules for the systems with $\alpha \geq 0.67$. We observed invariance in the interfacial ice percentage (Figure 5, top left) and greater percentage of I_c as compared to I_h percentage (Figure 5, bottom left) for all the cases. It can be noted that within initial clusters the plain AgI has greater I_h percentage in comparison to the defective surface which seems to be favourable for enhancement nucleation growth dynamics. Furthermore, we have shown the probability distribution of I_c to I_h ratio (Figure 5, in the right) for various defect systems. Here, the distribution for smooth AgI surface has mostly equal percentage of I_c and I_h. The surface with defects has greater I_c percentage as compared to plain AgI (for $\alpha \geq$ 0.67). Since the system with $\alpha < 0.67$ do not nucleate within the considered time, polymorph distribution analysis has not been conducted for these systems. Preceding works have asserted I_c/I_h ratio to be 2:1 for nanopore confinement at 195 K [51] and ≈ 2.5 for the nanodroplet at 200 K [68] as well as in cylindrical water droplet over nanotextured surface at 203 K [42]. The snapshots of the
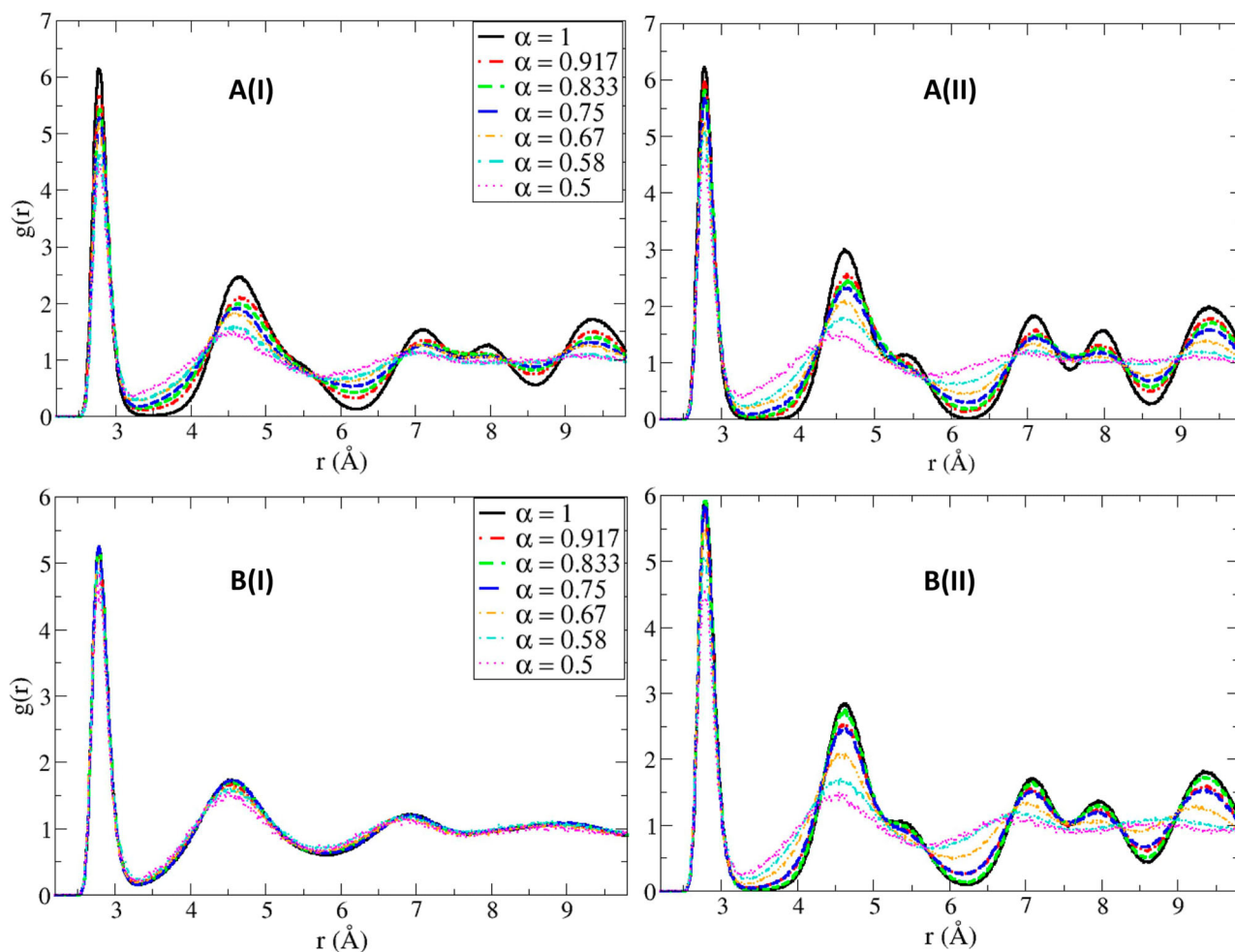
Figure 3. Oxygen–oxygen inplane radial distribution function for (A) first hydration layer (13.5–17 Å) and (B) second hydration layer (17–20.5 Å) over the following range of time (I) 5–15 ns and (II) 80–90 ns.

systems which nucleated are shown in Figures S2 and S3 in the supplementary. Table ST1 (in supplementary information) presents the overall ice percentage in the various systems at 150 ns and it can be noted that at a later period the changes in nucleation behaviour dies out. Hence, the defects influence the water layer close to the surface.

Additionally, we have shown the ice cluster size distribution (see Figure S4 in the supplementary) for the systems with $\alpha \geq 0.67$ at 60 and 120 ns in order to understand the influence of the defects on the cluster size distribution. It can be noted that the trend in the cluster distribution is similar for all the systems except for the variation in the size of the largest ice cluster for each defective surface. Figure S5 (in supplementary information) presents the average survival probability [69] (defined as the fraction of water molecules within the system) with respect to time. As expected, the decay rate of survival probabilities for the systems with $\alpha = 1$ and 0.833 is significantly faster than for the systems
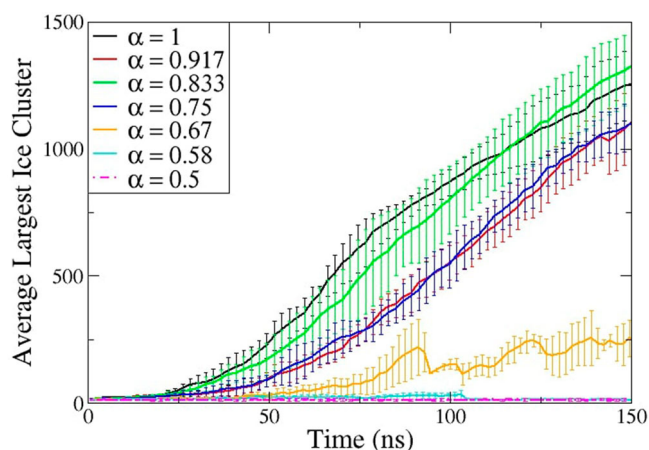

Figure 4. The average largest ice cluster size vs time plot along with the standard deviation for all the systems averaged over every configuration in which nucleation was observed.

with $\alpha = 0.917$ and 0.75. On the other hand, for α value 0.67, the decay rate of the survival probability is the slowest.
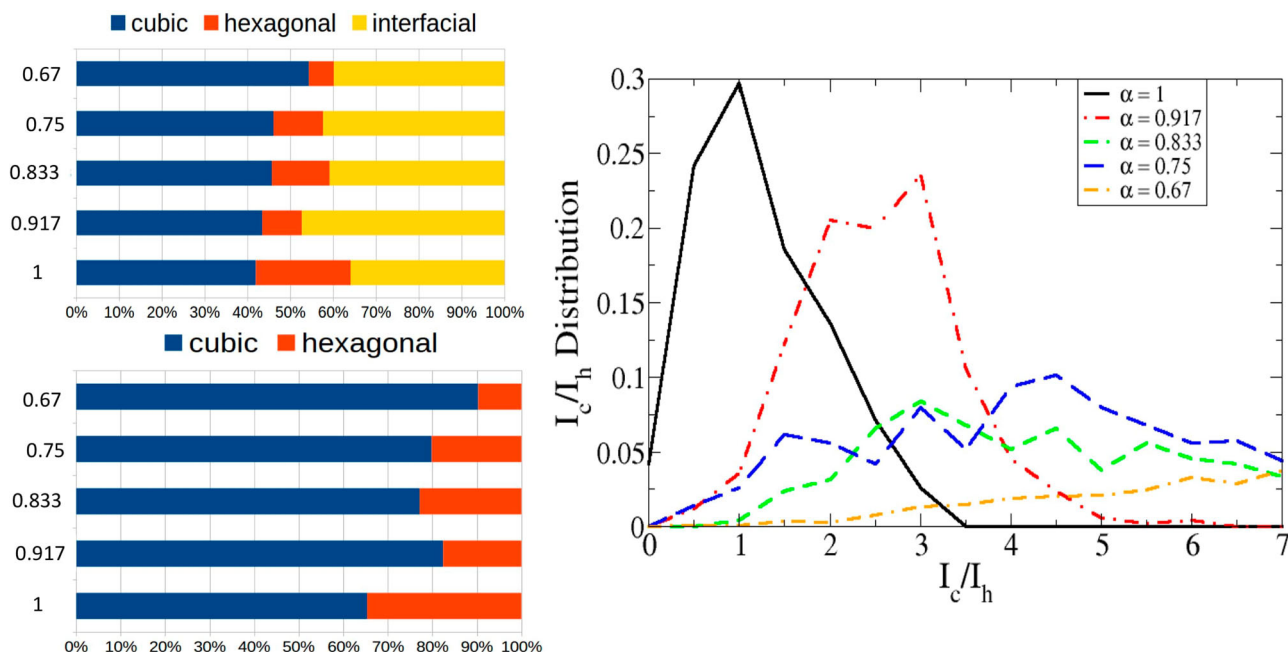
Figure 5. Left images show the early-time polymorph distribution (within the largest cluster size of 200 molecules) and the I_c and I_h distribution including interfacial ice is shown in the top and excluding interfacial ice is shown in the bottom. The plot on the right shows the probability distribution of I_c/I_h ratio for all the AgI substrates.
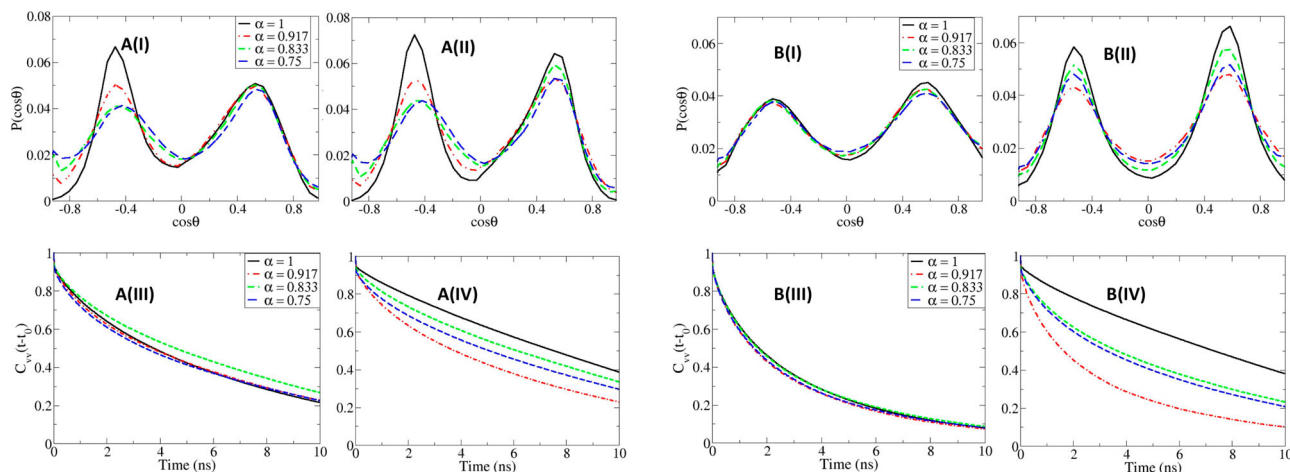

Figure 6. Orientational analysis of (A) first hydration layer (13.5–17 Å), (B) second hydration layer (17–20.5 Å) over the time range 5–15 ns (I, III) and 35–45 ns (II, IV). Here, A(I), A(II), B(I) and B(II) show the orientational distribution and A(III), A(IV), B(III) and B(IV) present the orientational correlation function.

The understanding of the variation in early nucleation behaviour with respect to the surface defect necessitates the analysis of the water molecules arrangement (in terms of dipole orientation) near the surface. Figure 6 displays the dipole orientational distribution (θ, the angle between water dipole and surface perpendicular as a function of $\cos\theta$) and the dipole orientation correlation of water for the first hydration layer and second hydration layer (i.e. 13.5–17 and 17–20.5 Å, respectively). It can be noticed that for both of the layers, two peaks around -0.468 and 0.525 ($\cos\theta$ value, which corresponds to

$\approx 120°$ and $\approx 60°$, respectively) appear. These orientations of water molecules have also been recognised in earlier studies [63,64] as the building blocks of the bi-layer ice over the surface and the promoter of the interlayer hydrogen bonding. Consequently, sharper the distribution at these orientation greater will be the orderliness of water molecules. For the first hydration layer, the nature of the first peak (see Figure 6A(I)) broadened with increasing defect size. However, there is no significant change in peak height with time (Figure 6A(II)). It can be inferred that this peak depends on the interaction
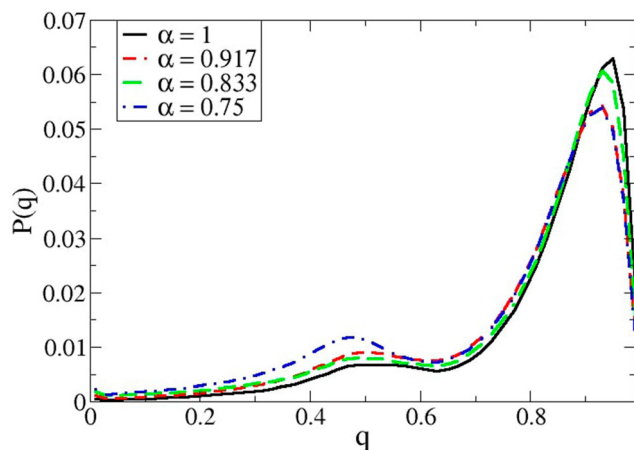
Figure 7. Tetrahedral order parameter distribution within 13.5–20.5 Å over the time range of 5–45 ns.

between surface atom and interfacial water and as a result, the peak height decreases with increasing defect size. In case of the second hydration layer (Figure 6B(I)), the angle distributions are broad (within the time range of 5–15 ns) which indicates the absence of water layering. However, with increasing time (for 35–45 ns, in Figure 6B(II)) variation in peak height is observed. The

growth in peak height is slightly apace for the surface with $\alpha = 1$ and 0.833, signalling relatively ordered orientational arrangement as compared to other systems comparison to $\alpha = 0.917$ and 0.75.

Figure 6A(III, IV) and B(III, IV) exhibits the dipole orientation correlation (see Equation (2)) which is related to the stability of hydrogen bond network (HBN) that aids the water to ice transition [65]. Figure 6A(III) and B(III) depicted that before nucleation (i.e. 5–15 ns) correlation decays fast along with an insignificant variation for all the systems. However, with the progression of nucleation (i.e. time range 35–45 ns, Figure 6A(IV) and B(IV)) the decay is slow indicating strong HBN stability in the order of $\alpha = 1 > 0.833 > 0.75 > 0.917$. Analogous results have been remarked in some of the prior studies where strong hydrogen bonding leads to sluggish decay of the correlation [70] and stable HBN enhances ice nucleation [65]. The greater HBN stability can also be supported by the distribution of tetrahedral order parameter (q) [71,72] as shown in Figure 7 (here, $q = 1$ denotes perfect tetrahedral network and $q = 0$ marks random mutual arrangement of water molecules, i.e. an ideal gas). The tetrahedrality close to the surface follows the order of $\alpha = 1 > 0.833 > 0.75 > 0.917$. Thus, the slow decay
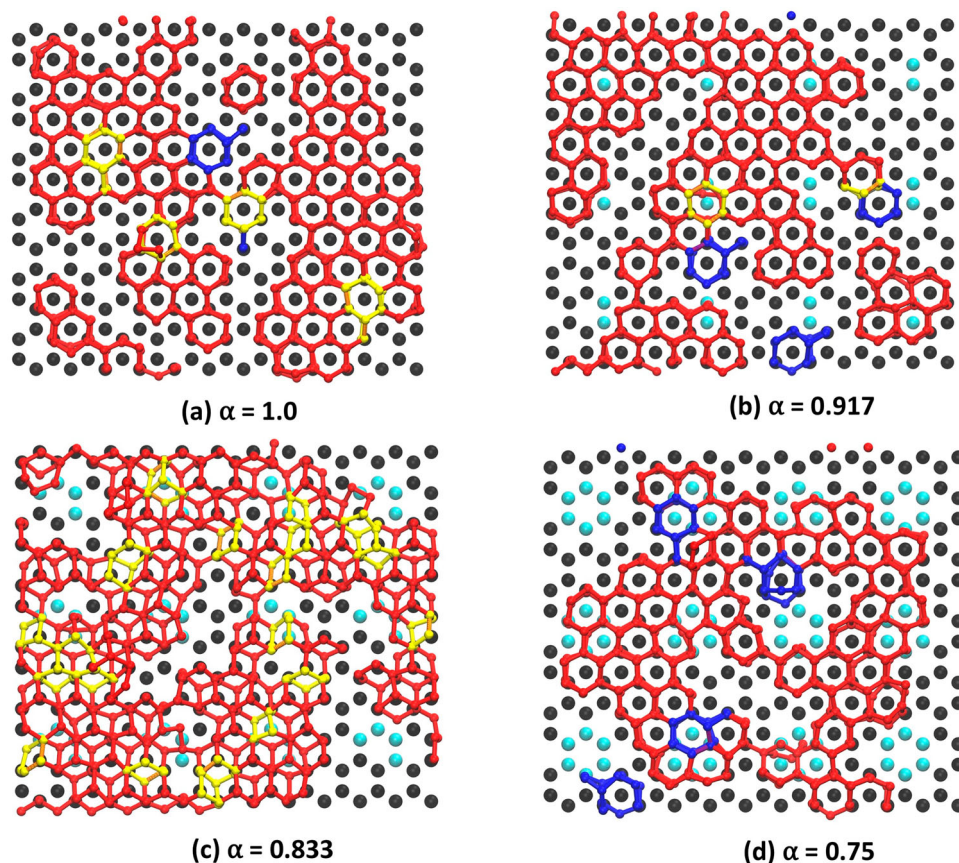

(a) α = 1.0

(b) α = 0.917

(c) α = 0.833

(d) α = 0.75

Figure 8. Top view of the first two layers and the surface coverage of ice formed at 100 ns. Hexagonal cages are in red, mixed cages are in yellow and double diamond cages are in blue. No DDCs are present for $\alpha = 0.833$.
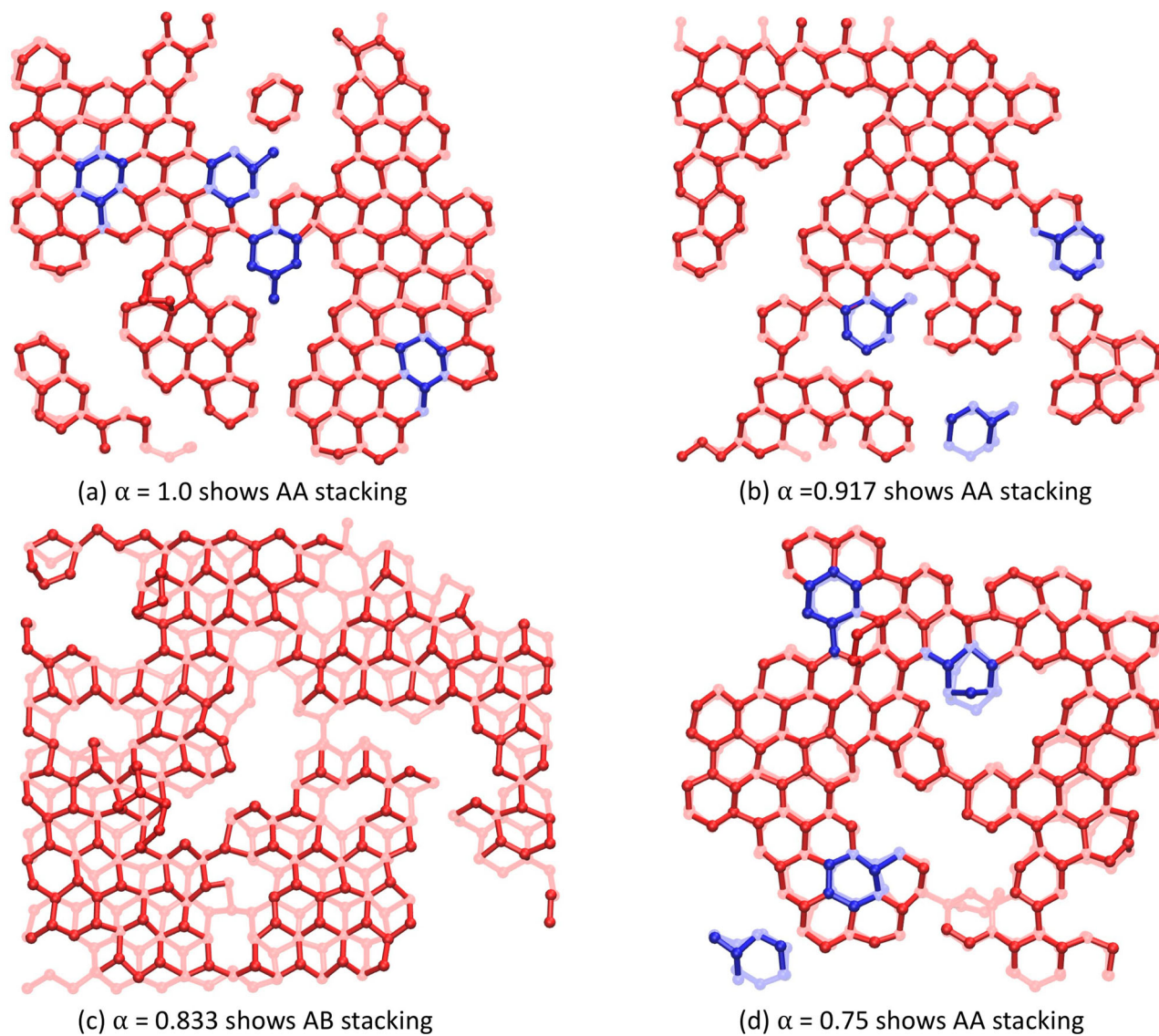
(a) α = 1.0 shows AA stacking

(b) α =0.917 shows AA stacking

(c) α = 0.833 shows AB stacking

(d) α = 0.75 shows AA stacking

Figure 9. Stacking of HC (red) and DDC (blue) structures over each defect for the first two layers. The faded colour represents the lower layer.
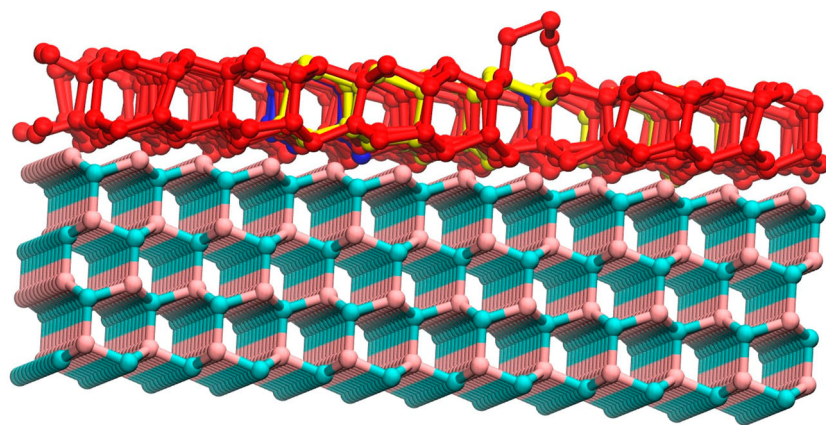

Figure 10. Representative snapshot showing the exact match of HC rings (red) with the hexagonal AgI surface, with DDC (blue) and mixed (yellow) rings visually demarcated. The template mismatch of DDC and mixed rings with respect to the surface is evident compared to the templating effect shown by underlying surface and HCs.

in dipole orientation correlation and greater value of tetrahedrality of the interfacial water enhances the ice nucleation ability.

To quantify the results of the HBN correlations, the structures which constitute the network itself is of great interest. As reported in the literature [54], the network of shortest distance based rings for such supercooled systems is essentially equivalent to the HBN. Starting with the six-membered primitive rings obtained from King's shortest path criterion [73], we then apply reductions [54] arising from considering the properties of the strongly hydrogen bonded network of ice. The results of this topological analysis, visualised in Figure 8 and in Figure S6 (supplementary), are intuitively pleasing and logically consistent. The primitives shown are classified as either DDCs, HCs or MCs, depending on a geometric criterion [54], as constituents of I_c, I_h or both, respectively. From Figure 8, we infer that the defects do not promote the formation of cages. The stacking of layers over the system with the $\alpha = 0.833$ surface defect (Figure 8(c)) differs from the other systems. This is clarified in Figure 9 where the layers are distinguished by the saturation of colours (a lighter shade is used to represent the lower layer and darker for the layer above). Here we define AA stacking to represent systems where the second layer forms approximately above the atoms of the first layer (Figures 9(a,b,d)), while AB stacking shows the second layer is not formed directly over the atoms of the first layer (Figure 9(c)). It is evident that the lower layer is not aligned for the system with $\alpha = 0.833$ as it shows AB stacking which may account for the complete lack of DDCs formed. Figure 10 depicts the side view of the plain AgI surface structure and the cages formed in the layers near the surface. Visual inspection of this figure shows the similarity of HCs and the AgI surface structure,

while DDCs and MCs are distorted with respect to the AgI hexagonal rings. It is evident from Figure 10 and 8 that structural instabilities reduce the available stable-nucleating surface and inhibit the growth of ice. It is pertinent to note that there are no complete rings observed within any of the defects in accordance with CHILL analysis [51], which shows no ice-like molecule inside the defect as well.

At 100 and 200 ns, the distributions of topological constructs in the first layers of all nucleating systems, namely $\alpha = 1.00, 0.917, 0.833, 0.75$ are shown in Figure 11. These times are significant as at 100 ns the layers considered are solid as per the radial distribution function of Figure 3 and at 200 ns, more than half the volume of the simulation box is in the solid phase. Figure 11 is a cluster graph at these instants of time, displaying the absolute number of each kind of ring structure formed with respect to the defect size. It is evident, and in accordance with previous literature [38,54], that the HCs are greater in number. However, the proliferation of these is enhanced by the presence of a substrate which matches their structural configuration. It is clearly seen from Figure 4 that the growth dynamics of the systems with $\alpha = 1$ and $\alpha = 0.833$ are similar. From Figure 11(a,b), we assert that this is due to the complete absence of purely cubic growth faces in the layers. The composition of the first two layers remains constant, and though the systems vary in their overall ice type compositions, these layers are not significantly altered or reformed. There is a complex interplay of these factors, and it is evident that the relative amounts of the cages account for the trends. The template matching of the $\alpha = 1$ and $\alpha = 0.833$ systems is strengthened by the fact that though the system with $\alpha = 0.917$ has more HCs than the $\alpha = 0.833$ system, it has a greater amount of MC and DDC structures, thus accounting for
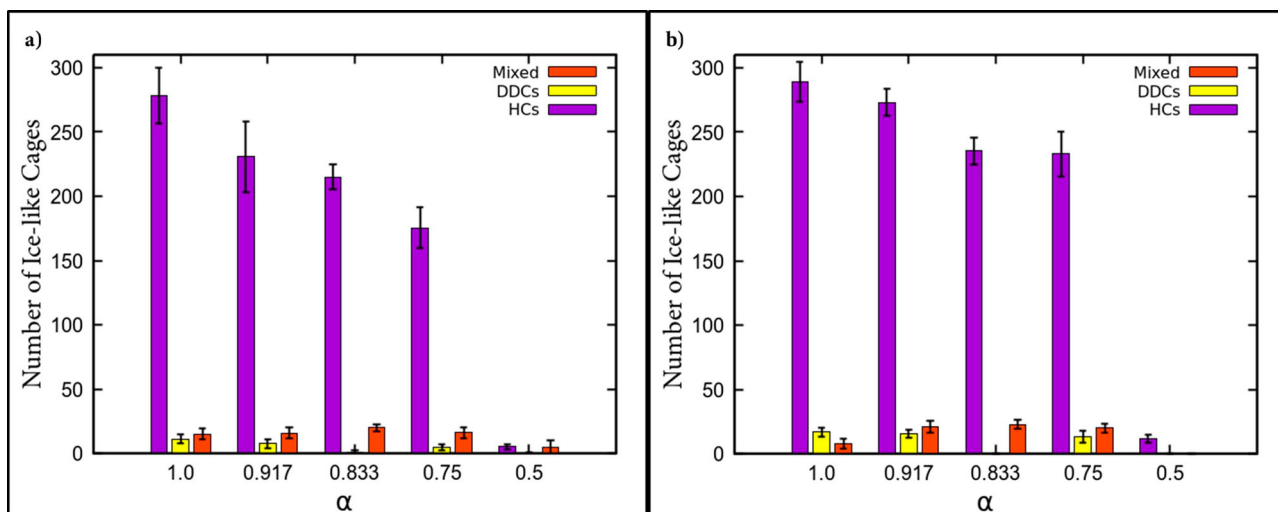

Figure 11. Distribution of the HC and DDC network for the first few layers with standard error at (a) 100 ns and (b) 200 ns.

the behaviour in Figure 4. Furthermore, it is important to note that the MC structures may precipitate either hexagonal or double diamond cage growth. This duality of purpose is shown in Figure 11, where it evident that over 100 ns of steady nucleation the MC structures in the $\alpha = 0.75$ system have been converted to HCs, while the system with $\alpha = 0.917$ shows a greater increase in DDCs. We assert that the topology effects for AA stacking systems, being as they are over a single layer, only effect the early time dynamics, and thus do not show the inhibition of nucleation shown by a surface with large defects ($\alpha < 0.67$). These are evident by the formation of DDC cages which changes the effective HC growth area seen in Figure 8. The cages formed at the surface are inferred to be stable (varying $< 5\%$ from 100 to 200 ns) are appropriately classified by the topological network criterion. For the system with AB stacking the effect of the defect is diminished, not only due to the DDC/HC ratio but also due to the enhanced coverage of the surface with ice-like cages. The systems with AA stacking are more strongly influenced by defect size. We suspect that the initial structures formed during the freezing of the first few layers may be a significant factor in determining nucleation efficiency, and posit that this 'template mismatch' corresponds to a retardation of the freezing process.

5. Conclusion

Ice nucleation on silver iodide surface incorporated with defects has been investigated using atomistic MD simulation and compared with the nucleation on plain AgI surface at 240 K temperature. We observe that the defects affect the arrangement of water molecules close to the surface while subsequent layers are not significantly influenced. From the average largest ice cluster size analysis, it is clear that the AgI surface without any defect shows early nucleation. Furthermore, the early-time polymorph distribution (within the largest cluster size of 200 molecules) demonstrates that the systems with defects have a greater cubic ice fraction than the plain AgI surface. The variation in the defect size has no effect on the cluster size distribution of ice. The orientational distribution exhibits a preference of the water dipole angle towards orientation ($\approx 60°$ and $\approx 120°$) for all the cases and the systems with $\alpha = 1.0$ and 0.833 show relatively greater intensity for these orientations than other systems with defect. This tends to enhance the propensity for the formation of ice-like structures. From the orientational correlation function, we perceive that the plain AgI surface induces the most stable hydrogen bond network (which influences the ice nucleation) followed by the surface with $\alpha = 0.833$. For other surface fractions

(i.e. $\alpha = 0.75$ and 0.917), this network is relatively less stable within both the first hydration layer and second hydration layer. The tetrahedrality for the strongly networked systems is also observed to be greater closer to the surface. The trends in the largest ice cluster, with respect to the lack of inhibition of the growth of the system with $\alpha = 0.833$, have been exhaustively examined. The topology in terms of ring structures and the layer stacking has been observed and quantified. The network of the first two layers is shown to be the determining factor in the inhibition of the defect systems. Specifically, we conclude that the existence of the DDCs shows a template mismatch effect and cause instabilities which are directly correlated to the near-surface layers, as they are not seen to be relevant at longer time-scales. These cages are structures which do not conform to the AgI's hexagonal surface, unlike the hexagonal cages. The system with $\alpha = 0.833$ has no pure cubic building blocks (DDC) and also shows AB stacking, while on non-defective AgI surface the most number of hexagonal cages are observed. We assert that the early nucleation dynamics is a strong function of the full topological connectivity of the first few surface layers. The effectiveness of AgI as a nucleating agent is disrupted by the formation of ice-like structures especially purely cubic blocks (DDCs) which cannot take advantage of the templating effect of the Ag exposed β-AgI surface. In other words, the ice nucleation is suppressed by the surface defects in case the DDC to HC ratio is unfavourable, or when the MC cages tend to evolve into DDC structures.

ORCID

Rohit Goswami http://orcid.org/0000-0002-2393-8056

References

[1] I. Coluzza, J. Creamean, M.J. Rossi, H. Wex, P. Aaron Alpert, V. Bianco, Y. Boose, C. Dellago, L. Felgitsch, J. Fröhlich-Nowoisky, H. Herrmann, S. Jungblut, Z.A. Kanji, G. Menzl, B. Moffett, C. Moritz, A. Mutzel, U. Pöschl, M. Schauperl, J. Scheel, E. Stopelli, F. Stratmann, H. Grothe and D.G. Schmale III, Atmosphere **8**, 138 (2017).

[2] G. Vali, Nucl. Atmos. Aerosols **1996**, 271–279 (1996).

[3] G. John Morris and E. Acton, Cryobiology **66** (2), 85–92 (2013).

[4] T. Kojima, T. Soma and N. Oguri, Theriogenology **30** (6), 1199–1207 (1988).

[5] B. Li and D.W. Sun, J. Food Eng. **54** (3), 175–182 (2002).

[6] R. Geidobler, S. Mannschedel and G. Winter, J. Pharm. Sci. **101** (12), 4409–4413 (2012).

[7] W. Gao, D. Smith and D. Sego, Cold Reg. Sci. Technol. **29** (2), 121–133 (1999).

[8] W. Gao, D. Smith and D. Sego, Cold Reg. Sci. Technol. **31** (1), 13–26 (2000).

[9] M.D. Petters and T.P. Wright, Geophys. Res. Lett. **42** (20), 8758–8766 (2015).

[10] P.R. Field and A.J. Heymsfield, Geophys. Res. Lett. **42** (21), 9512–9520 (2015).

[11] G. Petzold and J.M. Aguilera, Food Biophys. **4** (4), 378–396 (2009).

[12] R.L. Apodaca, D.M. Huff and W.R. Simpson, Atmos. Chem. Phys. **8** (24), 7451–7463 (2008).

[13] D. Axisa and T.P. DeFelice, Atmos. Res. **178–179**, 114–124 (2016).

[14] C. Hoose, J.E. Kristjánsson, J.P. Chen, A. Hazra, C. Hoose, J.E. Kristjánsson, J.P. Chen and A. Hazra, J. Atmos. Sci. **67** (8), 2483–2503 (2010).

[15] P.J. DeMott, A.J. Prenni, X. Liu, S.M. Kreidenweis, M.D. Petters, C.H. Twohy, M.S. Richardson, T. Eidhammer and D.C. Rogers, Proc. Natl. Acad. Sci. **107** (25), 11217–11222 (2010).

[16] F.T. Lynch and A. Khodadoust, Prog. Aerosp. Sci. **37** (8), 669–767 (2001).

[17] J. Laforte, M. Allaire and J. Laflamme, Atmos. Res. **46** (1–2), 143–158 (1998).

[18] Z. Zhang and X.Y. Liu, Chem. Soc. Rev. **47** (18), 7116–7139 (2018).

[19] P. Guo, Y. Zheng, M. Wen, C. Song, Y. Lin and L. Jiang, Adv. Mater. **24** (19), 2642–2648 (2012).

[20] H.A. Stone, ACS Nano **6** (8), 6536–6540 (2012).

[21] M. Jung, T. Kim, H. Kim, R. Shin, J. Lee, J. Lee, J. Lee and S. Kang, Appl. Surf. Sci. **351**, 920–926 (2015).

[22] D. Rosenfeld and W.L. Woodley, Nature **405** (6785), 440–442 (2000).

[23] C.H. Twohy and M.R. Poellot, Atmos. Chem. Phys. **5** (3), 3723–3745 (2005).

[24] C. Hoose, U. Lohmann, R. Erdin and I. Tegen, Environ. Res. Lett. **3** (2), 025003 (2008).

[25] B.J. Murray, D. O'Sullivan, J.D. Atkinson and M.E. Webb, Chem. Soc. Rev. **41** (19), 6519 (2012).

[26] D. Rosenfeld, U. Lohmann, G.B. Raga, C.D. O'Dowd, M. Kulmala, S. Fuzzi, A. Reissell and M.O. Andreae, Science **321** (5894), 1309–1313 (2008).

[27] A. Kiselev, F. Bachmann, P. Pedevilla, S.J. Cox, A. Michaelides, D. Gerthsen and T. Leisner, Science **355** (6323), 367–371 (2017).

[28] F. Lüönd, O. Stetzer, A. Welti and U. Lohmann, J. Geophys. Res. **115** (D14), D14201 (2010).

[29] C. Marcolli, B. Nagare, A. Welti and U. Lohmann, Atmos. Chem. Phys. **16** (14), 8915–8937 (2016).

[30] T. Li, D. Donadio, G. Russo and G. Galli, Phys. Chem. Chem. Phys. **13** (44), 19807 (2011).

[31] T.F. Whale, M. Rosillo-Lopez, B.J. Murray and C.G. Salzmann, J. Phys. Chem. Lett. **6** (15), 3012–3016 (2015).

[32] M. Raju, A. Van Duin, and M. Ihme, Sci. Rep. **8** (1), 3851 (2018).

[33] L. Lupi and V. Molinero, J. Phys. Chem. A **118**, 43 (2014).

[34] L. Lupi, A. Hudait and V. Molinero, J. Am. Chem. Soc. **136**, 3 (2014).

[35] N. Hiranuma, O. Möhler, K. Yamashita, T. Tajiri, A. Saito, A. Kiselev, N. Hoffmann, C. Hoose, E. Jantsch, T. Koop and M. Murakami, Nat. Geosci. **8** (4), 273–277 (2015).

[36] D. O'Sullivan, B.J. Murray, J.F. Ross, T.F. Whale, H.C. Price, J.D. Atkinson, N.S. Umo and M.E. Webb, Sci. Rep. **5** (1), 8082 (2015).

[37] M. Fitzner, G.C. Sosso, S.J. Cox and A. Michaelides, J. Am. Chem. Soc. **137** (42), 13658–13669 (2015).

[38] S.A. Zielke, A.K. Bertram and G.N. Patey, J. Phys. Chem. B **119** (29), 9049–9055 (2015).

[39] A.K. Metya and J.K. Singh, J. Phys. Chem. C **122** (15), 8277–8287 (2018).

[40] J.K. Singh and F. Müller-Plathe, Appl. Phys. Lett. **104**, 124709 (2014).

[41] A.K. Metya and J.K. Singh, Mol. Simul. **45** (4–5), 394–402 (2019).

[42] A.K. Metya, J.K. Singh, and F. Müller-Plathe, Phys. Chem. Chem. Phys. **18** (38), 26796–26806 (2016).

[43] B. Vonnegut, J. Appl. Phys. **18** (7), 593–595 (1947).

[44] W.G. Finnegan, S.K. Chai, W.G. Finnegan and S.K. Chai, J. Atmos. Sci. **60** (14), 1723–1731 (2003).

[45] S. Shevkunov and J.K. Singh, J. Mol. Liq. **264**, 150–164 (2018).

[46] S.V. Shevkunov, Colloid J. **81** (1), 50–63 (2019).

[47] S.V. Shevkunov, Colloid J. **81** (1), 64–76 (2019).

[48] S.V. Shevkunov, Colloid J. **79** (5), 685–700 (2017).

[49] Y. Bi, B. Cao and T. Li, Nat. Commun. **8**, 15372 (2017).

[50] P.J. Steinhardt, D.R. Nelson, and M. Ronchetti, Phys. Rev. Lett. **47** (18), 1297–1300 (1981).

[51] E.B. Moore, E. de la Llave, K. Welke, D.A. Scherlis and V. Molinero, Phys. Chem. Chem. Phys. **12** (16), 4124 (2010).

[52] A.H. Nguyen and V. Molinero, J. Phys. Chem. B **119** (29), 9369–9376 (2015). 00034.

[53] C.G. Salzmann, P.G. Radaelli, B. Slater and J.L. Finney, Phys. Chem. Chem. Phys. **13** (41), 18468 (2011).

[54] A. Haji-Akbari and P.G. Debenedetti, Proc. Natl. Acad. Sci. **112** (34), 10582–10588 (2015).

[55] G.C. Sosso, T. Li, D. Donadio, G.A. Tribello and A. Michaelides, J. Phys. Chem. Lett. **7** (13), 2350–2355 (2016).

[56] J.L.F. Abascal, E. Sanz, R. García Fernández and C. Vega, J. Chem. Phys. **122** (23), 234511 (2005).

[57] B.N. Hale and J. Kieferb, J. Chem. Phys. **73** (2), 923–933 (1980).

[58] S. Plimpton, J. Comput. Phys. **117** (1), 1–19 (1995).

[59] W. Humphrey, A. Dalke and K. Schulten, J. Mol. Graph. **14** (1), 33–38 (1996).

[60] J.P. Ryckaert, G. Ciccotti and H.J. Berendsen, J. Comput. Phys. **23** (3), 327–341 (1977).

[61] S. Nosé, J. Chem. Phys. **81** (1), 511–519 (1984).
[62] W.G. Hoover, Phys. Rev. A **31** (3), 1695–1697 (1985).
[63] B. Glatz and S. Sarupria, Langmuir **34** (3), 1190–1198 (2017).
[64] B. Glatz and S. Sarupria, J. Chem. Phys. **145** (21), 211924 (2016).
[65] C. Li, X. Gao and Z. Li, J. Phys. Chem. C **121** (21), 11552–11559 (2017).
[66] M. Fitzner, G.C. Sosso, F. Pietrucci, S. Pipolo and A. Michaelides, Nat. Commun. **8** (1), 2257 (2017).
[67] A. Bose, A.K. Metya and J.K. Singh, Phys. Chem. Chem. Phys. **17** (35), 23147–54 (2015).
[68] J.C. Johnston and V. Molinero, J. Am. Chem. Soc. **134** (15), 6650–6659 (2012).
[69] P. Wilson, A. Heneghan and A. Haymet, Cryobiology **46** (1), 88–98 (2003).
[70] J. Chanda and S. Bandyopadhyay, J. Phys. Chem. B **110** (46), 23482–23488 (2006).
[71] J.R. Errington and P.G. Debenedetti, Nature **409** (6818), 318–321 (2001).
[72] P. Chau and A.J. Hardwick, Mol. Phys. **93** (3), 511–518 (1998).
[73] D.L. Evans and S.V. King, Nature **212** (5068), 1353–1354 (1966).